ADVANCED MATERIALS
www.advmat.de

Multispectral Molecular Chiral Barcoding

*Aritra Biswas, Pablo Cencillo-Abad, and Debashis Chanda**

More than half of pharmaceutical drugs in use are chiral, necessitating accurate techniques for their characterization. Enantiomers, molecules with mirrored symmetry, often exhibit similar physical traits but possess distinct chemical and biological implications. This study harnesses the strong light-matter interaction induced by "superchiral" light to perform Surface-Enhanced Infrared Absorption (SEIRA) induced vibrational circular dichroism measurements in the mid-infrared spectral region. Utilizing a nanopatterned pixelated array of achiral plasmonic nanostructures, the system allows unique identification of enantiomers and biomolecules. Tunability of plasmon resonance facilitates spectral variation of the optical chirality over a wide infrared range, enabling development of a unique chiral "barcoding" scheme to distinguish chiral molecules based on their infrared fingerprint. This simple, yet robust sensor presents a low-cost solution for chiral mapping of drugs and biomolecules.

1. Introduction

Chirality, the intrinsic property of asymmetry, is a fundamental aspect of our world, sparking renewed interest across various research disciplines, including chemistry, biology, physics, medicine, and pharmaceutics in recent decades. It describes the property of an object being non-overlapping with its mirror image. Almost half of all designed medical drugs along with a plethora of naturally occurring biomolecules are chiral, resulting in an ever-growing demand for efficient detection and classification techniques.[1] Chirality can exist at the smallest molecular bonding level (tryptophan, glucose, limonene to name a few), or can exist at a large-scale structurally complex level such as in supramolecular conformations[2] (proteins, DNAs, peptide chains, etc.). Certain pairs of chiral molecules, known as enantiomers, exist in both mirror imaged forms, and although they exhibit similar physical properties, they may have vastly different chemical or biological implications with regards to reactivity,[3] potency, and functionality.

Chiroptical measurement techniques such as optical rotatory dispersion (ORD) and circular dichroism (CD) have been excellent candidates for identification of such complex chiral structures and molecules, where polarized light having an associated spin-momentum (such as in circularly polarized light) interacts differently with chiral molecules, enabling the identification and reliable determination of their chiral properties. However, reliable CD spectral measurement of low molecular concentrations, especially in the infrared domain, is difficult owing to weak extinction cross-sections due to dimensional mismatch between target molecules and excitation wavelength. Hence, higher concentration and larger volume (longer interaction path length) are required for reliable CD measurements. Since the introduction of the conserved pseudoscalar quantity known as optical chiral density (C),[4] a significant interest has been generated in the scientific community to develop a better understanding of chiral light-matter interaction mechanisms.[5–8] Several techniques for chiral detection have been reported over the last few years,[9–13] employing both plasmonic[14–24] and photonic[25–28] platforms to amplify optical response through enhanced chiral interaction. Though a significant focus has been put in enhancing CD responses in the ultra-violet (UV), visible, and near-infrared regions, very few have shown applications in the mid-infrared (mid-IR) domain,[29–31] where almost all molecules exhibit unique vibrational absorption "fingerprints". This region carries important information about chemical bonds as well as macromolecular arrangements of large molecules like proteins. Though there have been few attempts to develop techniques for the detection[32–34] and identification[35] of such molecular mid-IR fingerprints, one main limitation yet to overcome is the inability to distinguish spectrally similar molecules. Many long-chain biomolecules have similar vibrational spectra in the mid-IR region due to them having similar amino-acid blocks (e.g., Amide I and II regions) but different three-dimensional block orientations and arrangements which imparts spatial asymmetry, making them chiral-active. Several large macromolecules (proteins, amino acids, enzymes) have higher order secondary and tertiary structural forms. These structural arrangements cannot be distinguished by simple spectral absorption analysis, but are important as they can unveil information about disorders and misfolding in proteins, and accurate structural understanding may enable diagnosis of

A. Biswas, D. Chanda
CREOL, The College of Optics and Photonics
University of Central Florida
4304 Scorpius St., Orlando, FL 32816, USA
E-mail: Debashis.Chanda@ucf.edu
A. Biswas, P. Cencillo-Abad, D. Chanda
NanoScience Technology Center
University of Central Florida
12424 Research Parkway Suite 400, Orlando, FL 32826, USA
D. Chanda
Department of Physics
University of Central Florida
4111 Libra Drive, Physical Sciences Bldg. 430, Orlando, FL 32816, USA

The ORCID identification number(s) for the author(s) of this article can be found under https://doi.org/10.1002/adma.202409565

DOI: 10.1002/adma.202409565

several neurodegenerative diseases[36,37] like dementia, Parkinson's diseases, etc. Vibrational circular dichroism (VCD) identify such structural arrangements uniquely by determining the asymmetry in molecular interaction with oppositely-handed circularly polarized light (CPL).[38,39] However, conventional bulk-phase VCD suffers from the large mismatch between the detection wavelength and the molecular dimension, leading to extremely weak differential signals[39] typically of the order of 10^{-5} – 10^{-6}, which enforces the need for high concentration and longer detection pathlengths to obtain a reliable signal. Therefore, the need to have a detection scheme that would enable sensitive and unique identification of chiral arrangements from low concentration analytes in the mid-IR vibrational fingerprint domain would greatly advance the current state-of-the-art.

In this article, we report a method of chiral encoding based on a pixelated array of spectrally detuned achiral plasmonic sensors.[40–42] The sensor pixels exhibit far-field near-perfect resonant absorption in the mid-IR spectral domain with a Q-factor limited only by the cavity phase matching and metallic losses. Under broadband illumination, the hybrid metallic hole-disk arrangement coupled to a resonant cavity generates simultaneous near-field electric and magnetic mode enhancements at the mid-IR resonance.[40] Intriguingly, when the illumination is circularly polarized (CP), these electric and magnetic dipolar modes exhibit phase-lagged temporal rotation which leads to the generation of a localized, single-handed, and homogeneously enhanced near-field optical chiral density (C) whose spin direction (+1 or −1) is determined by the handedness of the incident circular polarization.[42] Owing to the symmetry and the localized nature of C, the proposed system does not exhibit any inherent far-field circular dichroic response. The array pixels are optimized to generate resonant responses linearly covering the mid-IR spectral domain from 3333 cm^{-1} to 1400 cm^{-1} ($\lambda = 3.3$ µm to 6.4 µm) which encompasses the molecular fingerprint region of many known chiral analytes and biomolecules. This near-field enhancement in electromagnetic field and optical chirality provides an excellent platform to perform surface-enhanced infrared absorption (SEIRA) induced surface-enhanced vibrational circular dichroism (SEVCD) of chiral-active molecules within a single measurement setup at the same time. The retrieved SEIRA and SEVCD response from the combined (plasmonic + molecular) system is analyzed and encoded to create a "chiral barcode" that uniquely represents the molecules' vibrational chiral fingerprint. As an example, this mechanism of chiral molecular barcoding is utilized to distinguish an enantiomeric pair of small molecules. We also show the applicability of this platform to generate chiral barcodes for distinguishing spectrally similar chiral biomolecules. The measured SEVCD signal shows an enhancement of ≈13 orders of magnitude compared to standard VCD spectroscopy, after normalizing for pathlength and concentration as reported in our earlier work.[43] Unlike other chiral sensing platforms that require chiral nanostructures of varying degrees of asymmetry[29,31] which can be challenging to replicate, the proposed platform's inherent symmetry overcomes this issue, thus significantly simplifying the fabrication process. The sensors are easy to fabricate, involving simple nanoimprint lithography and a series of deposition steps, making them very robust since the final device is entirely made of a sturdy dielectric and an inert metal. Moreover, measurements require very low volumes of analytes, enabling unique and reliable identification of chiral molecules from ultra-low concentrations. Integration with fast-scanning spectral apparatus would even enable real-time tracking and barcoding of changes in protein structures and kinematics. We envision that the versatility of this platform would make it a crucial tool for artificial drug and biomolecular identification, which has many applications in medical research, drug designing and pharmaceuticals.

2. Results

Figure 1a shows a schematic representation of the pixelated multispectral sensing platform. The sensing surface consists of 25 pixels arranged in a 5 × 5 array, each having a periodic array of 3D gold-based hole and disk units, stacked on top of an underlying dielectric photonic cavity. The individual pixels cover an area of 1 × 1 mm^2 as shown in Figure 1b, with a fixed hole diameter (D) and inter-hole periodicity (P). The ratio between D and P has been fixed at 2/3 for all pixels to minimize fabrication variability and facilitate ease of scalability. The spectral resonance response of the pixelated system is tuned across a linear range of wavelengths in the mid-IR region. The pixelated sensor shown here is configured to cover a range from 3.3 µm (∼ 3000 cm^{-1}) to 6.4 µm (1538 cm^{-1}), where most drugs and large biomolecules have their vibrational absorption fingerprints. Spectral tunability is controlled by a monotonous scaling parameter S as shown in Figure 1c, with the system's corresponding far-field reflectance spectra shown in Figure 1e. For simplicity, we refer to the pixels by integer values ranging from N = 1 to 25, denoting the pixel numbers from top left to bottom right (Figure 1d, top left). Figure 1d (right top and bottom) shows the top view scanning electron microscope (SEM) images for two of the pixels corresponding to the 1st (red square) and 25th (blue square). The plasmonic array is coupled to an underlying resonant cavity formed by a reflector at the bottom, as seen in the cross-sectional SEM image in Figure 1d (left bottom). The hybrid coupling between the top localized surface plasmon resonance (LSPR) mode of the 3D hole-disk array and the photonic cavity resonant mode generates a sharp and narrow hybridized resonance characterized by a near-perfect absorption (dip in reflectance) in the far-field spectral domain. The system's geometrical parameters are optimized in a way to have the lowest (first) order resonance response in the mid-IR region, and the subsequent pixel array responses are scaled accordingly. Figure 1e shows the far-field reflectance spectra in the mid-IR for the bare nanostructured pixels. The corresponding reflectance response after adsorption of a chiral active molecule on the pixels is shown in Figure 1f, along with its inherent IR absorption spectra (Figure 1f, top). The corresponding calculated chiral barcodes based on the integrated dissymmetry are shown in Figure 1g,h, respectively, where the dissymmetry factor (g) is denoted as $g = 2(A^+ - A^-)/(A^+ + A^-)$ corresponding to the absorption (A) for right (+) and left (-) CPL. While the generated barcode corresponding to a bare sensor shows null response (Figure 1g), the one with the adsorbed chiral molecule shows a distinct response with highlighted pixels, characteristic of the molecule's chiral behavior.

On excitation with CPL, simultaneous electric and magnetic modes are generated in the near-field at resonance.[40–42] These resonant modes are analogous to a rotating dipole with a spatially

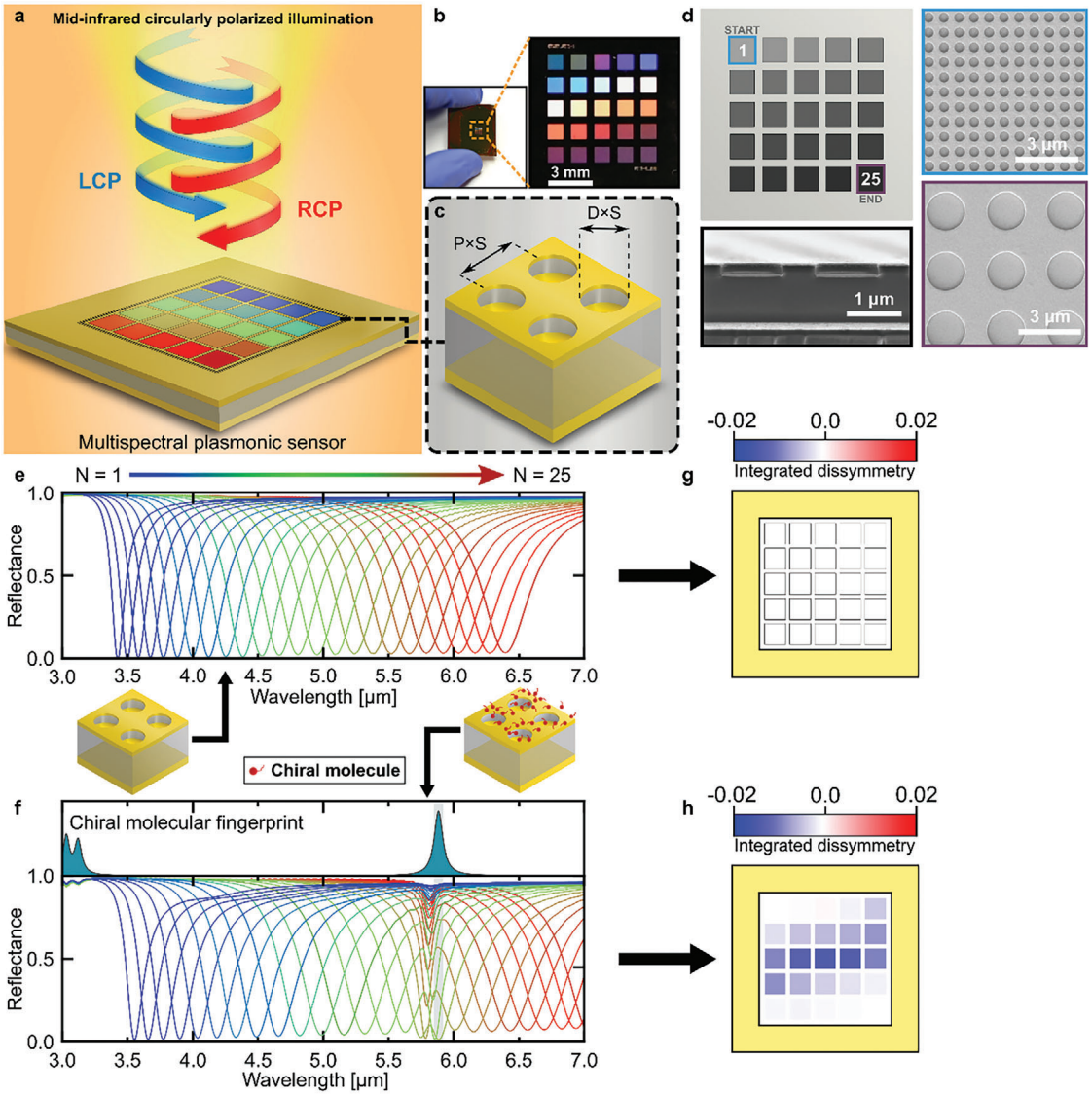

Figure 1. Multispectral pixel-based chiral barcoding system. a) Schematic of the multispectral chiral barcoding system. b) Photograph of a fabricated sensor (left) and magnified version showing the pixelated surface (right), with each pixel having a dimension of 1×1 mm^2. c) Representation of a unit cell of the plasmonic sensor. d) Pixel configuration and corresponding scanning electron microscope images of pixels 1 (top right) and 25 (bottom right), labelled accordingly. Bottom left shows cross-section SEM of geometry. e) Spectral reflectance and g) corresponding dissymmetry map of the pixelated sensor without any molecule; and f,h) with adsorbed molecules, with the molecular vibrational absorption fingerprint show in the top part of (f).

symmetric magnitude over the patterned surface. The polarity of this near-field is flipped based on the handedness of the excitation CPL as can be observed from the finite difference time domain (FDTD) predictions in **Figure** 2a. Figure 2b,c show the simulated time-averaged electric and magnetic field intensity enhancements respectively at resonance for one of the pixelated arrays under CPL excitation. The magnetic mode enhancement is stronger near the hole region, while the electric field strength peaks near the disk region within the geometry. The field intensity distribution is identical for both handedness of the circularly polarized excitation.[42] This unique spatial distribution generates an enhanced chiral density C, described as a conserved pseudoscalar that quantifies the magnitude of "helical twist" of light.[4] C is defined for a monochromatic light source as $C(\omega) = -\frac{\epsilon_0 \omega}{2} Im(\boldsymbol{E}^*.\boldsymbol{B})$, where $\boldsymbol{E}^*$ is the complex conjugate of the local electric field, $\boldsymbol{B}$ is the corresponding magnetic field, ω is the frequency and ϵ_0 is the permittivity of free space. Figure 2a shows the distribution of enhanced optical chirality over the plasmonic system under left (LCP) and right (RCP) handed circularly polarized illumination. The optical chirality enhancement (C_{nf}) is defined as C normalized to the free-space optical chiral density (C_{CPL}). This exhibits two important qualities of the system, a) the optical chirality enhancement has a homogenous magnitude that solely depends on the rotational handedness of the excitation, and b) the enhancement is purely a near-field effect and does not impart a far-field CD or ORD response to the system. This allows suppression of the structure-induced asymmetry and ensures that any asymmetric response on molecular adsorption is only

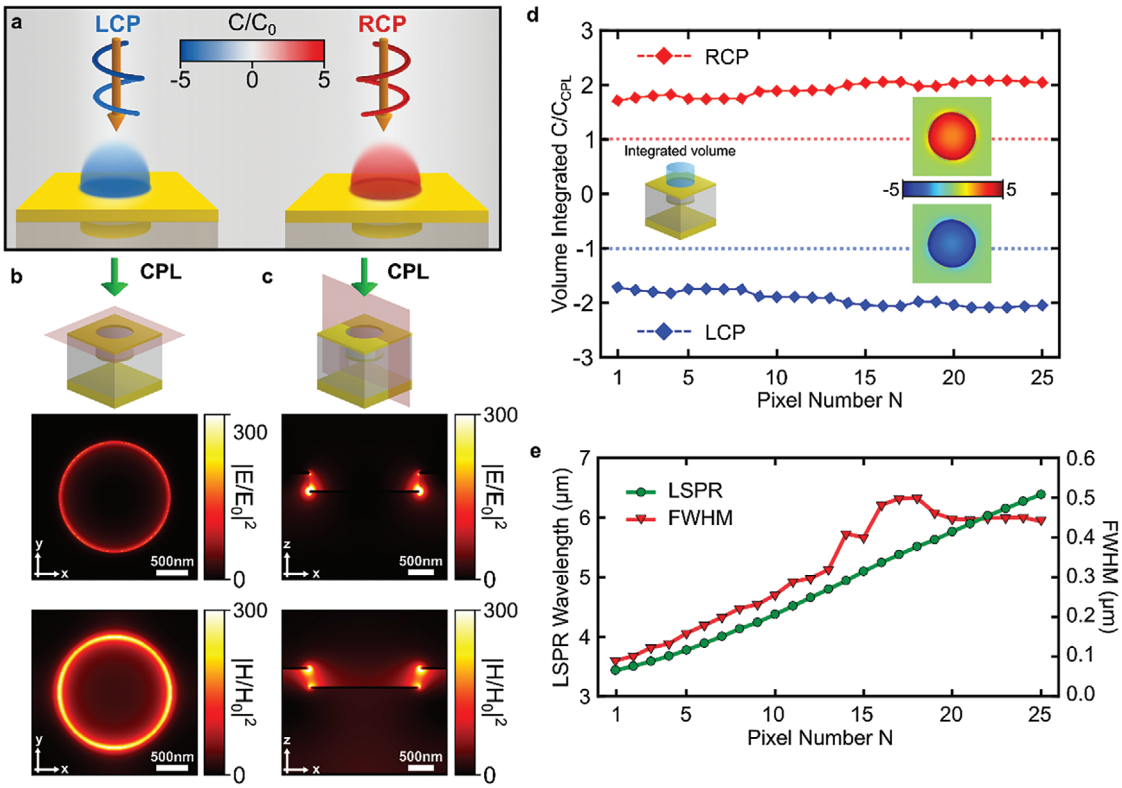

Figure 2. Electromagnetic response of the system. a) 3D near-field optical chiral density over the unit cell of the sensor for left- and right- CPL. b,c) 2D profiles of electric (|E/E0|2) and magnetic (|H/H0|2) field intensity enhancement at (b) 3 nm above the hole and (c) cross-section through the center for one of the pixels (N = 13) at the first-order localized surface plasmon resonance (LSPR). d) Volume integrated optical chirality up to a lateral height of 200 nm above the surface for the pixelated plasmonic system. e) The corresponding LSP resonance wavelength and full width at half maximum (FWHM).

due to the chiral properties of the adsorbed analytes. Moreover, the resonance tuning capability allows simultaneous spectral tuning of the near-field electric and chiral density modes. Figure 2d shows the volume integrated optical chirality enhancement at resonances as a function of the pixel number, for which the details of calculation are provided in the supplementary information. The corresponding resonance wavelengths and full width half maxima (FWHM) are shown in Figure 2e. The vertical distance of integration is taken up to 200 nm above the top metallic layer, as this encompasses typical thickness ranges of the adsorbed molecular layers. The inset in Figure 2d shows a representative 2D-distribution of C_{nf} for one of the pixels, 2 nm above the top surface layer for RCP (top) and LCP (bottom) illumination. The near-field exhibits high chiral enhancement ($C_{nf} > 1$) over the sensing layer, indicating an enhanced chiral density magnitude at the first order resonances for all pixelated arrays.

Since the proposed sensing platform has a bottom mirror, the incident light is either absorbed by the top plasmonic system or reflected back to free space. As a result, the absorption spectrum can simply be calculated as $A = 1\text{-}R$, where A and R denote the absorption and reflection coefficients. Typical spectral measurements are performed over a macroscopically significant area over which the chiral molecules are adsorbed. As such, the adsorbed molecules can be considered as a randomly oriented isotropic ensemble. The absorption rate for chiral molecules of such an isotropic system in the presence of monochromatic CPL having frequency ω is given as:[4]

$$A^{(+/-)} = \frac{\omega}{2}\left(\alpha''\left|\tilde{\boldsymbol{E}}\right|^2 + \chi''\left|\tilde{\boldsymbol{B}}\right|^2\right) \pm G''\omega \mathrm{Im}\left(\tilde{\boldsymbol{E}}^*.\tilde{\boldsymbol{B}}\right) \quad (1)$$

Here, superscripts + and – indicate RCP and LCP excitation, α'' and χ'' are the imaginary parts of the electric polarizability and magnetic susceptibility of the chiral molecule respectively, while G'' denotes the mixed electric-magnetic dipolar response which is non-zero for chiral active molecules, and $\tilde{\boldsymbol{E}}$ and $\tilde{\boldsymbol{B}}$ are the complex local electric and magnetic fields at the molecule respectively. For a general non-magnetic system (valid for most naturally occurring molecules), the expression for dissymmetry factor g becomes:[4,7]

$$g = \left(\frac{G''}{\alpha''}\right)\left(\frac{2C}{\omega\varepsilon_0|\boldsymbol{E}|^2}\right) \quad (2)$$

The contribution from the terms involving magnetic susceptibility is ignored as most molecules are non-magnetic in nature. The dissymmetry factor depends on both the optical property of the molecules (first term in parenthesis) and the electromagnetic properties of the surrounding field (second term in parenthesis). The dimensional mismatch between molecules and excitation wavelengths (few nm vs 100's of nm) renders the first term very

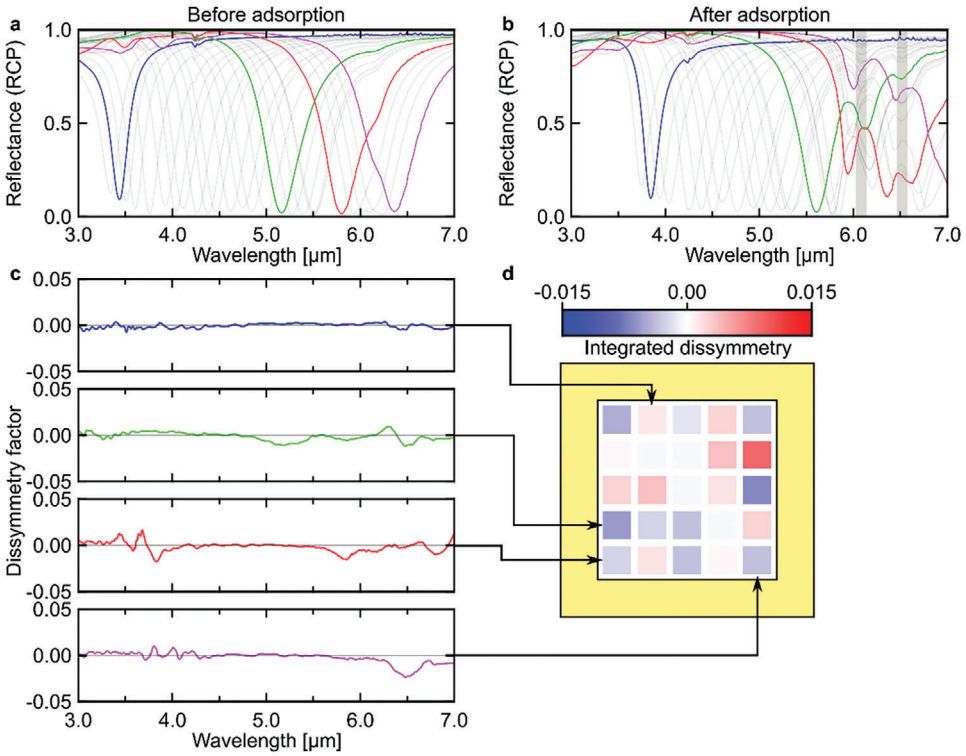

Figure 3. Mechanism of barcoding. a) System far-field response before and after molecular adsorption. For four pixels with various degrees of overlaps (S = 2, 13, 21, 25). b) Corresponding dissymmetry for the four pixels. c) Corresponding barcode map.

small. Therefore, by proper engineering of the nanostructured system, the field-dependent term can be improved by enhancing *C*. This constitutes the main advantage of our proposed plasmonic platform, providing simultaneous enhancements in near-field $\tilde{\boldsymbol{E}}$ and *C*. Additionally, the $\tilde{\boldsymbol{E}}$ enhancement is more localized near the bottom disk region (Figure 2b, middle) than the top hole, which consequently would lead to an overall enhancement in the dissymmetry factor at resonance for the coupled molecule-plasmonic system (**E** being in the denominator).

On molecular adsorption, an asymmetric CD response is generated when there is a significant overlap between the molecular absorption and the plasmonic resonance. **Figure** 3a,b show the experimentally measured far-field spectral reflectance for the pixelated array sensor before and after molecular layer adsorption respectively (shown here just for RCP excitation). Here, we use biomolecule lysozyme as an example to demonstrate chiral barcode formation. Lysozyme has two prominent absorption bands corresponding to Amide I (1658 cm^{-1}) and Amide II (1530 cm^{-1}), highlighted in Figure 3b as two gray bars for better visualization. Note that for the bare sensor in Figure 3a, there is a slight resonance broadening at longer wavelengths (e.g., red and purple curves in Figure 3a) due to the inhomogeneous linewidth broadening of the LSPR mode. Nevertheless, both LCP and RCP excitations produce identical resonances resulting in zero far-field CD. On molecular adsorption, the far-field reflectance *R* changes (Figure 3b) which eventually indicates a change in absorption *A* between LCP and RCP excitation. The difference in LCP and RCP absorption is represented in the dissymmetry factor *g*. Primarily, the dissymmetry factor enhances intensity differences by normalizing with respect to the detected signal, providing a quantitative analysis of the degree of differential absorption. Four cases of various degrees of overlaps between the molecular absorption and sensor resonances are highlighted as blue, green, red and magenta color plots in Figure 3a,b. The molecular adsorption is accompanied by a spectral shift that depends on the local changes in refractive index and molecular density on the sensor surface, a common effect that occurs due to the reduction in the light's phase velocity in effective near-field media, lowering the wavevector and leading to change of resonance condition to lower energies, effectively seen as a spectral red-shift. The spectral splitting, however, occurs due to the coherent interference between two resonant absorption modes that generates a plasmon-induced transparency (PIT)[44–46] at the overlap location. This occurs due to a degeneracy-induced interference between a sub-radiant (dark) and a super-radiant (bright) mode, which in this case corresponds to the weak molecular absorption and the sensor's strong plasmon resonance, respectively. The strength of the induced splitting is dictated by the molecular density and the degree of spectral overlap between the molecule and the corresponding pixels' resonant absorptions. On excitation with oppositely-handed CPL, different spectral dissymmetry factors are observed for all the pixels. These variations in spectral overlap would lead to different degrees of coupling between the near-field chiral enhancement and the inherent molecular chirality, leading to variations in the measured VCD far-field response. Figure 3c shows the baseline subtracted dissymmetry factors for four pixels corresponding to the four color-coded spectra in Figure 3b. A weaker overlap would produce a relatively weak SEVCD

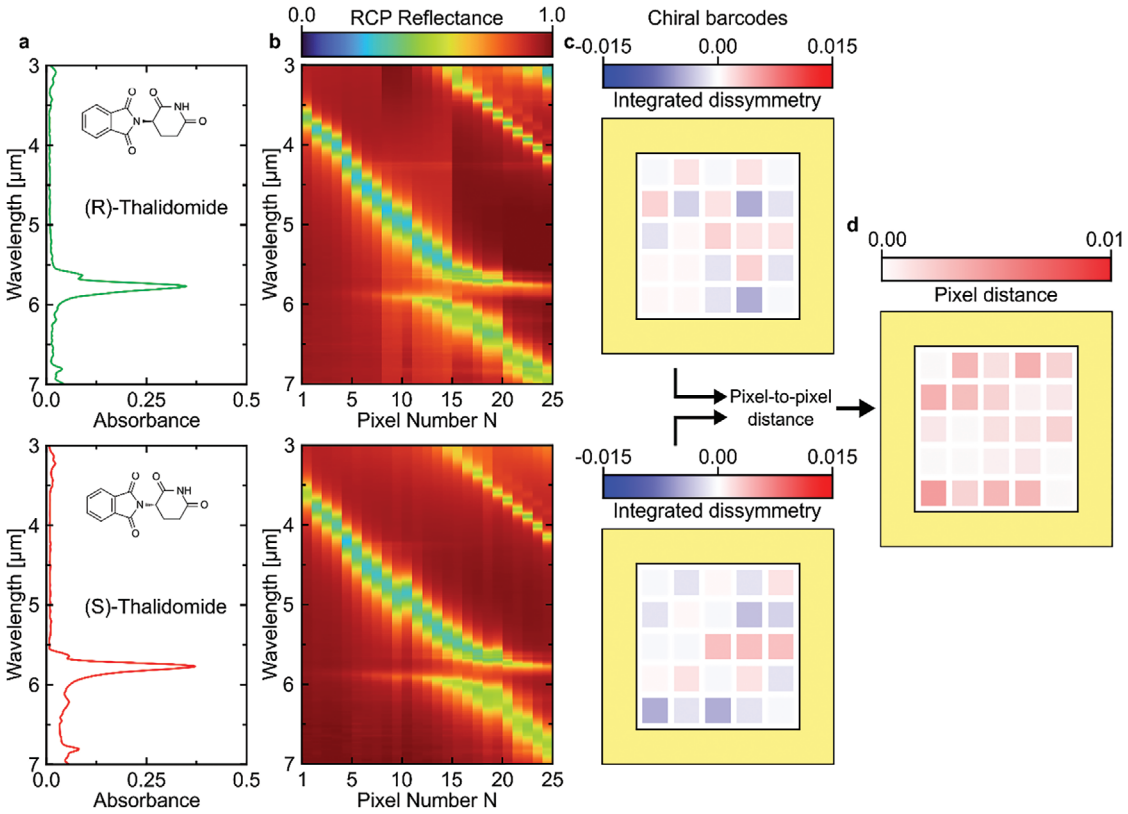

Figure 4. Chiral barcoding-based discrimination of enantiomers. a) Infrared reflection-absorption spectroscopy (IRRAS) measurement of adsorbed thin-film thalidomide enantiomers (R – (top) and S – (bottom)) on gold coated substrates. b) Corresponding reflectance heat-maps for R – and S – thalidomide-adsorbed pixelated metasurfaces for RCP illumination. c) Color barcoding of integrated dissymmetry for thalidomide enantiomers, R – (top) and S – (bottom). d) Pixel-to-pixel distance for the barcodes, showing dissymmetry distances for each pixel.

response as seen in the dissymmetry spectra (Figure 3c). Additionally, near-field chiral coupling determines the magnitude as well as the sign of the observed dissymmetry response ($+g/-g$). As mentioned before, due to the geometrical symmetry of the system, the dissymmetry response should be zero in absence of chiral molecules for all pixels. However, due to slight imperfections in fabrication of the sensors, experimentally determined dissymmetry spectra exhibit slight non-zero values near resonances even without a molecular layer. This is taken as a baseline ($g_{w/o.\ molecule}$) and is subtracted from the calculated dissymmetry from the molecule-coated sensor's responses ($g_{w.\ molecules}$) to get a final background removed dissymmetry spectra ($g = g_{w.\ molecules} - g_{w/o.\ molecule}$), containing only chiral information from the molecule. We specify a quantity g_{int}, defined as $g_{int} = \int g d\lambda$, where the integration is over a spectral region encompassing the molecule-induced perturbation in the sensor's spectral response. Non-overlapping or weakly overlapping pixels would produce negligible g_{int}. For subsequent pixels, the dissymmetry spectra would be modified accordingly, leading to different magnitudes and signs for g_{int}, depending on the near-field chiral interaction. The associated g_{int} values are color-coded and represented as a "chiral barcode", that is uniquely assigned to a chiral molecule as shown in Figure 3d. The barcode pattern depends on the degree of molecule-sensor pixel spectral absorption overlap. If M color codes can be discerned and there are N pixels, then M!*N! molecules can be uniquely identified based on N sensor pixels.

The first approach shown is to utilize this barcoding platform to perform enantio-selectivity, i.e., to identify enantiomers. For this study, thalidomide enantiomers are chosen as target molecules for classification. **Figure** 4a shows the spectral absorbance of (R)-thalidomide (top) and (S)-thalidomide (bottom) adsorbed on optically thick gold-coated substrates in the region of interest, measured using infrared reflection-absorption spectroscopy (IRRAS). A thin layer of thalidomide molecules is adsorbed on the surface of the multispectral sensor array, the adsorption process is described in the Methods Section. The determined thickness, verified with an average topology measurement of the adsorbed sensor surface using atomic force microscopy, is ≈160 nm. The corresponding SEIRA-based reflectance for the RCP excitation, for both (R) and (S)-thalidomide, is shown as a 2D heatmap in Figure 4b (corresponding LCP excitation heatmaps are shown in Figure S7, Supporting Information). A PIT-induced splitting can be observed at the region of sharp molecular absorption (≈5.79 μm, corresponding to the C = O stretch vibration in thalidomide) indicating strong near-field coupling between the molecular absorption response and the underlying sensor plasmon resonance. The corresponding generated barcodes for the two enantiomeric molecules are shown in Figure 4c. The barcode for (R)-thalidomide (Figure 4c, top) shows mostly red pixels, indicating that the "weighted" dissymmetry is mostly positive. Similarly, the barcode for (S)-thalidomide, as expected, exhibits an opposite

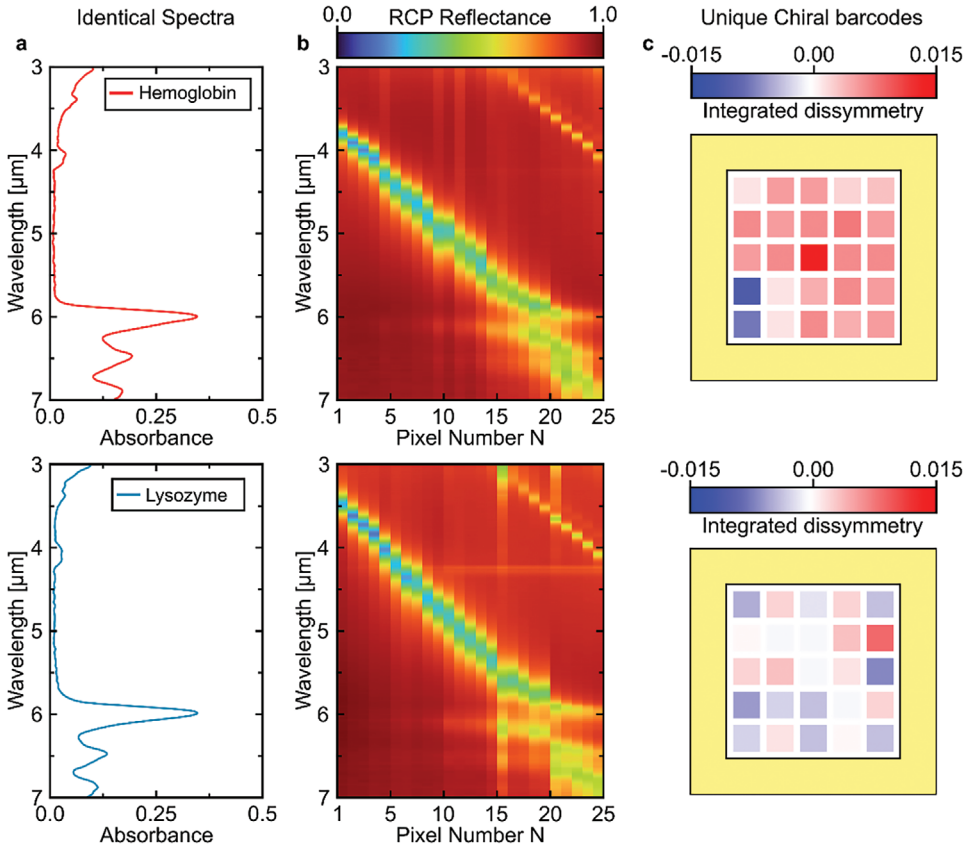

Figure 5. Chiral barcoding-based classification of spectroscopically similar biomolecules. a) IRRAS measurement of hemoglobin (top) and lysozyme (bottom) on gold coated substrates. b) Corresponding RCP reflectance heatmaps for adsorbed molecules on pixelated metasurfaces for hemoglobin (top) and lysozyme (bottom). c) Color barcoding of integrated dissymmetry for hemoglobin (top) and lysozyme (bottom).

response, as seen in Figure 4c (bottom). For a fair comparison, the same sensor has been used for both measurements after thorough cleaning (Methods Section) and verification of cleaned spectral response. The pixel-to-pixel distance is represented as a differential barcode in Figure 4d, indicating the difference in the integrated dissymmetry value for each pixel. A brighter color, corresponding to a larger pixel-to-pixel distance, indicates greater chiral response dissymmetry at that spectral location.

In the next study, we demonstrate the identification of larger biomolecules that vary in their physical and biological properties but have similar vibrational absorption fingerprints. Such biomolecules cannot be identified by simple SEIRA-based techniques but can be distinguished based on their chiral response. Hemoglobin and Lysozyme were chosen as target proteins for this study. Hemoglobin, a protein found in red blood cells, facilitates transportation of oxygen in living beings,[47] while lysozyme is another lighter protein that helps in providing immunity against external microorganisms.[48] Hemoglobin (≈64 500 g mol^{-1}) is ≈4.5 times heavier than lysozyme (≈14 000 g mol^{-1}) while having a similar absorption profile in the mid-infrared region. **Figure 5a** shows the measured IRRAS for both biomolecules, hemoglobin (top) and lysozyme (bottom) adsorbed on gold substrates, following the procedure described in the Methods Section. Both have similar absorption spectra in the mid-infrared domain, with absorption bands at 1640 and 1580 cm^{-1}. The corresponding SEIRA-based 2D heatmaps for RCP excitation on molecular adsorption are shown in Figure 5b (LCP excitation is shown in Figure S8, Supporting Information), exhibiting a similar trend in terms of the PIT-based splitting observed at the locations of resonant overlaps. The subtle reflectance differences observed in pixels 15 to 25 are due to slight differences in film thicknesses, experimental conditions, and sensor used during the measurements. However, the spectral splitting at the position of molecular and LSPR overlap for both cases occur at the same locations due to both biomolecules having similar absorption fingerprint, hence it cannot be used to distinguish them uniquely. While the concentration for both biomolecular solutions are same, the absorbed hemoglobin layer corresponds to a thickness of ≈120 nm, while for the lysozyme, the average surface thickness is measured to be ≈100 nm, as determined by AFM-based averaged surface topology measurements. The appropriate baseline corrected integrated dissymmetry-based barcodes are shown in Figure 5c corresponding to hemoglobin (top) and lysozyme (bottom). Interestingly, the barcodes show distinct values for both biomolecules, which uniquely identify them depending on their chiral interaction with spectrally varying pixels. Hemoglobin shows integrated dissymmetry with mostly positive values as indicated by the reddish pixels. On the other hand, the trend for lysozyme seems to be more balanced with higher wavelength pixels showing a blueish

color, indicating a mostly negative value of integrated dissymmetry. As the pixel resonances, and in turn the enhanced chiral fields, are swept over the molecular fingerprint region, different degrees of overlap occur between the molecular chiral response and the plasmon-enhanced chiral near-field, leading to differences in the chiral light-matter interactions, which are reflected in the (sign and magnitude) integrated dissymmetry values. Note that for some pixels with plasmon resonances at the higher wavelengths, certain higher-order resonances appear in the range of interest (Figures 4b and 5b), which also generate enhanced chiral near-field due to simultaneous higher order modes interaction. But these resonances are non-overlapping with any of the vibrational fingerprint regions in question and hence would contribute negligibly to the overall dissymmetry.

3. Conclusion

The ability to utilize the concept of optical chirality for sensitive detection and classification of chiral active molecules opens a new paradigm for molecular identification. Here, we have proposed and experimentally demonstrated a plasmonic multispectral pixelated array exhibiting hybrid localized plasmon resonance in the mid-IR wavelength range to create unique chiral-based molecular barcodes based on their absorption fingerprints. The nanostructured platform generates simultaneously enhanced localized and symmetric electric and magnetic near-field mode at resonance on excitation with CPL. This in turn generates enhanced near-field optical chiral density which is homogeneous and whose sign can be controlled by the polarization handedness of the excitation without requiring multiple separate chiral nanostructures. The system's spectral resonance, and in turn its enhanced chiral response, can be tuned by changing the system's geometrical parameters, which has been utilized here to generate a multispectral array-based sensor.

SEVCD, or VCD in general, provides valuable information about molecular structure and conformations that would not be possible in the UV-visible region. Owing to our system's symmetry and local nature of the enhancements, we demonstrated SEIRA and SEVCD measurements simultaneously using this platform, enabling us to not only extract information about the molecules IR chemical properties, but also provide structural information that facilitates enantiomeric discrimination and higher-order structure identification based on a unique chiral barcoding scheme. To demonstrate the efficacy of the scheme, we apply this platform to experimentally distinguish between an enantiomeric pair of small molecules and two spectroscopically similar large biomolecules based on their unique chiral barcodes. The fabrication process is simple and amenable to batch production using common techniques like nanoimprint lithography and standard deposition methods. Furthermore, the response of the nanostructured system can be readily extended through parametric scaling to encompass a broader range, from mid to far infrared regions, aligning with the absorption fingerprint of the targeted chiral drugs or biomolecules. The enhanced resonant chirality combined with geometrical spectral tunability of the nanostructured pattern allows us to span a large region for reliable molecular barcoding. We envision that this platform can be integrated to dynamically monitor real-time changes in protein dynamics and create unique libraries of chiral barcodes based on their IR fingerprints. Such a versatile system can be a useful tool for identification and classification of biomolecules and synthetic drugs, having relevance in chemical, medical, and pharmaceutical research.

4. Experimental Section

Sensor Fabrication: A schematic representation of the fabrication process steps is shown in Figure S1 (Supporting Information). The initial process started with the fabrication of a master pattern consisting of the original pixelated pattern of scaled nanohole arrays. The master pattern design consisted of 25 pixels arranged in a 5 × 5 array, with each pixel consisting of a square array of nanoholes of size 1 × 1 mm^2. The diameter and periodicity of the smallest nanohole array were 0.464 and 0.696 µm respectively (D/P = 2/3) and the subsequent pixels were scaled up accordingly by 5% increments. A poly di-methyl siloxane (PDMS) based stamp mold was made from the master pattern. Pristine microscope glass slides were cut, sonicated in acetone for 1 hour, and rinsed with iso-propyl alcohol (IPA) and deionized water respectively followed by drying with inert nitrogen. Electron beam (e-beam) evaporation was used to coat a 5 nm layer of titanium (Ti) acting as an adhesion promoter, a 100 nm film of gold (Au), and another 5 nm thin layer of Ti adhesion layer. An amorphous layer of silicon dioxide (SiO_2) was deposited by e-beam evaporation, with the thickness approximately being 1 µm. A diluted version of a negative photoresist SU-8 2000.5 (Kayaku Adv. Materials) was spin-coated on to the substrate, followed by thermal embossing of the previously fabricated PDMS stamp mold to transfer the nanohole array pattern on to the SU-8 photoresist. This was followed by UV-curing of the photoresist. Following this, the substrate was dry etched by reactive ion etching in an argon/trifluoromethane (Ar/CHF_3) environment at a 2:3 gas ratio to transfer the nanohole pattern from the photoresist onto the SiO_2 cavity. The etch recipe was priorly optimized to create excellent vertical side-walls with a vertical depth of ≈200 nm, necessary for subsequent directional deposition. Finally, a layer of 3 nm Ti followed by a 30 nm Au thin film was deposited via e-beam evaporation to create the top 3D-separated disks and nanoholes, thus concluding the sample making process. The surface spatial profile was mapped to verify the vertical depth of the underlying disk via atomic force microscopy (Figure S3, Supporting Information). Several multipixel sensors can be created in a single batch of fabrication.

Preparation of Chiral Molecular Thin Films: The chemicals and biomolecules used were as follows: (+)-Thalidomide (≥98% purity, #T150-10MG, Sigma Aldrich), (-)-Thalidomide (≥98% purity, #TG151-10MG, Sigma Aldrich), dimethyl sulfoxide (DMSO, #276855-1L, Sigma Aldrich), Hemoglobin Human (H7379-1G, Sigma Aldrich), Lysozyme (89833, Thermo-Scientific), Deuterium Oxide or Heavy water (D_2O,435767-100G, Sigma Aldrich). Both thalidomide enantiomers were diluted in 100 µL DMSO and kept at −20 °C to maintain potency prior to experiments. Fresh enantiopure dilutions of thalidomide at concentrations of 1 mM each were prepared and used in experimental spectral collection within 24 hours. Lysozyme and hemoglobin solutions were prepared in D_2O at appropriate dilutions to prepare 1 mM solutions each. Prior to adsorption, the sensor's surface was rinsed with acetone, isopropyl alcohol, and deionized water followed by blow-drying with nitrogen gas. The sensors were then treated in an oxygen (O_2) plasma environment to remove organic residues and improve wettability of surface. A scotch tape cut boundary was created around the sensor region, followed by drop-cast and spin coating at a low rotation speed for 30 seconds of the required chiral molecular solution. The sample was then gently warmed for 5 minutes and allowed to dry. This created a homogenous film of molecular coating on the measurement surface.

Experimental Characterization: The schematic of the detection setup is shown in Figure S5 (Supporting Information). The measurement apparatus consisted of a reflection-mode microscope (HYPERION 1000, Bruker Corp.) with a low numerical aperture (NA), 4× calcium fluoride (CaF_2) objective. This was coupled to a Fourier Transform Infrared (FT-IR) spectroscopy system (VERTEX 80, Bruker Corp.) that was configured

with a mid-infrared (MIR) globar thermal source and a KBr beamsplitter. A zinc selenide (ZnSe)-based broadband linear polarizer (LP) with its fast axis along the horizontal direction was placed along the FT-IR system's output beam path. This was followed by a motorized rotation stage (PRM1Z8, Thorlabs) mounted achromatic (4000-1429 cm^{-1}) quarter waveplate (Bernard Halle Nachfolger Gmbh) that converted the LP excitation to right or left CP excitation depending on the relative orientation of its fast axis with respect to the LP. The excitation light was normally incident on the sensor surface following which the reflected response was redirected to a cryo-cooled mercury-cadmium telluride (MCT) broadband IR detection. The response was estimated for both right and left CPL excitation, and the data collection and processing was performed with Bruker's processing software OPUS. Post-processing and barcode analysis of measured data was performed in MATLAB.

Infrared Reflection-Absorption Spectroscopy (IRRAS) Measurements: IRRAS measurements of the chiral molecules were performed with an infrared ellipsometry system (IR-VASE Mark II, J. A. Wollam Co.). Optically thick gold-coated glass slide substrates were sonicated in acetone and cleaned with IPA and deionized water. Solutions of the prepared chiral molecules were spin-coated on the Au films and dried to create thin-films. The adsorbed Au substrates were loaded onto the ellipsometer, and reflection measurements were performed at an incident angle of 80°. Prior to this, a reference measurement with bare Au substrate was performed. To ensure efficient signal collection only from the region of interest, the measurement region's surrounding was covered with lint-free roughened napkins (Kimwipes). The principle here was that the overall path length of incident light was increased enabling absorption measurements of thin films, down to monolayers. The film interacted with only the p-polarized light, and not the s-polarized one. Reflection (R) data was collected for R_{pp}, corresponding to p-polarization aligned polarizer and analyzer, and subsequently absorption (A) was calculated as $A = 1 - R$.

Reproducibility of Results: Prior to experiment, the sensors were cleaned thoroughly followed by O_2 plasma cleaning to improve surface wettability. Figure S6 (Supporting Information) depicts controlled experiments performed with three independent sensors in the absence of chiral molecules, showing similar reflectance maps and minimal variability in the generated barcodes. Measurements of each adsorbed sensor was performed twice, and new sensor adsorption measurement was performed three times for every chiral molecule. Hemoglobin-adsorbed sensors were difficult to clean, hence these sensors were measured only once, with new sensors used every time. Other sensors were cleaned thoroughly in acetone sonication bath for 5 minutes followed by the cleaning protocol described above. To verify reusability, cleaned sensors were spectroscopically measured and reproducibility verified.

The experiments were performed in a controlled laboratory environment at a regulated temperature with typical humidity of <40% to minimize atmosphere-induced variability. Prior to measurements, the system was kept on standby for 20 minutes to allow stabilization of the MIR source and the detector. The measurement region was purged with inert nitrogen gas every 10 minutes to minimize CO_2 interference. The measurements were averaged over 156 times to remove any background noise fluctuations.

The achromatic quarter waveplate (QWP) operates within the 2.5–7 µm (4000-1429 cm^{-1}) range. To minimize small inhomogeneity in uniform quarter-phase retardation over the broadband spectral range, separate baseline references were performed for RCP (+45° relative to LP) and LCP (−45° relative to LP) excitations on a gold reference substrate. These references were used for corresponding normalized measurements of the adsorbed chiral analytes (RCP baseline for RCP excitation, and LCP baseline for LCP excitation). The measured RCP and LCP reflectance spectra were then used to calculate the dissymmetry, which is now free from any retarder-induced artifacts. This guarantees that the excitation is mostly single-handed polarized for specific QWP angle.

Simulations and Modelling: The electromagnetic simulations of the reflection spectra and the local electric, magnetic, and chiral near-fields were performed using finite-difference time domain (Lumerical FDTD, *Ansys*) method which solved the Maxwell's equation numerically in the time domain using the Yee-cell method. Figure S2a (Supporting Information) shows the simulated reflectance spectral heatmap for the multispectral sensor, in comparison to the experimentally measured reflectance (Figure S2b, Supporting Information). The optical parameters (complex refractive indices) for Au and SiO_2 were determined by IR spectroscopic ellipsometry (IR-VASE Mark II, J. A. Wollam). Post-processing of the data to calculate the integrated near-field chiral enhancements was performed in MATLAB.

Supporting Information

Supporting Information is available from the Wiley Online Library or from the author.

Acknowledgements

This work at the University of Central Florida was supported by NSF grant no. ECCS-1800845.

Conflict of Interest

The authors declare no conflict of interest.

Author Contributions

D.C. and A.B. contributed to research design and conceptualization. A.B. performed the experiment. A.B. and D.C. performed data analysis. A.B., P.C.-A., and D.C. contributed to manuscript writing.

Data Availability Statement

The data that support the findings of this study are available from the corresponding author upon reasonable request.

Keywords

chirality, nanofabrication, plasmonics, SEVCD

Received: July 4, 2024
Revised: September 2, 2024
Published online:

[1] L. A. Nguyen, H. He, C. Pham-Huy, *Int. J. Biomed. Sci.* **2006**, *2*, 85.
[2] E. V. Belova, E. V. Semenova, V. A. Tverdislov, *Biophysics* **2022**, *67*, 374.
[3] J. H. Kim, A. R. Scialli, *Toxicol. Sci.* **2011**, *122*, 1.
[4] Y. Tang, A. E. Cohen, *Phys. Rev. Lett.* **2010**, *104*, 163901.
[5] C. He, G. Yang, Y. Kuai, S. Shan, L. Yang, J. Hu, D. Zhang, Q. Zhang, G. Zou, *Nat. Commun.* **2018**, *9*, 5117.
[6] H. Rhee, Y. G. June, J. S. Lee, K. K. Lee, J. H. Ha, Z. H. Kim, S. J. Jeon, M. Cho, *Nature* **2009**, *458*, 310.
[7] Y. Tang, A. E. Cohen, *Science* **2011**, *332*, 333.
[8] R. M. Kim, J. H. Huh, S. J. Yoo, T. G. Kim, C. Kim, H. Kim, J. H. Han, N. H. Cho, Y. C. Lim, S. W. Im, E. J. Im, J. R. Jeong, M. H. Lee, T. Y. Yoon, H. Y. Lee, Q. H. Park, S. Lee, K. T. Nam, *Nature* **2022**, *612*, 470.
[9] L. A. Warning, A. R. Miandashti, L. A. McCarthy, Q. Zhang, C. F. Landes, S. Link, *ACS Nano* **2021**, *15*, 15538.
[10] J. Mun, M. Kim, Y. Yang, T. Badloe, J. Ni, Y. Chen, C. W. Qiu, J. Rho, *Light: Sci. Appl.* **2020**, *9*, 139.

[11] S. J. Yoo, Q. H. Park, *Nanophotonics* **2019**, *8*, 249.
[12] L. Hu, Z. Sun, Y. Nie, Y. Huang, Y. Fang, *Laser Photon Rev.* **2022**, *16*, 2200035.
[13] E. Hendry, T. Carpy, J. Johnston, M. Popland, R. V. Mikhaylovskiy, A. J. Lapthorn, S. M. Kelly, L. D. Barron, N. Gadegaard, M. Kadodwala, *Nat. Nanotechnol.* **2010**, *5*, 783.
[14] M. Schäferling, N. Engheta, H. Giessen, T. Weiss, *ACS Photonics* **2016**, *3*, 1076.
[15] M. Schäferling, X. Yin, N. Engheta, H. Giessen, *ACS Photonics* **2014**, *1*, 530.
[16] E. Hendry, R. V. Mikhaylovskiy, L. D. Barron, M. Kadodwala, T. J. Davis, *Nano Lett.* **2012**, *12*, 3640.
[17] M. Schäferling, D. Dregely, M. Hentschel, H. Giessen, *Phys. Rev. X* **2012**, *2*, 031010.
[18] T. J. Davis, E. Hendry, *Phys. Rev. B Condens. Matter Mater. Phys.* **2013**, *87*, 085405.
[19] Y. Zhao, A. N. Askarpour, L. Sun, J. Shi, X. Li, A. Alù, *Nat. Commun.* **2017**, *8*, 14180.
[20] M. Hentschel, M. Schäferling, X. Duan, H. Giessen, N. Liu, *Sci. Adv.* **2017**, *3*, 1602735.
[21] W. Wu, M. Pauly, *Mater. Adv.* **2022**, *3*, 186.
[22] V. E. Bochenkov, T. I. Shabatina, *Biosensors* **2018**, *8*, 120.
[23] M. Hentschel, V. E. Ferry, A. P. Alivisatos, *ACS Photonics* **2015**, *2*, 1253.
[24] S. Liu, X. Ma, M. Song, C. Y. Ji, J. Song, Y. Ji, S. Ma, J. Jiang, X. Wu, J. Li, M. Liu, R. Y. Wang, *ACS Nano* **2021**, *15*, 19535.
[25] E. Mohammadi, A. Tavakoli, P. Dehkhoda, Y. Jahani, K. L. Tsakmakidis, A. Tittl, H. Altug, *ACS Photonics* **2019**, *6*, 1939.
[26] E. Mohammadi, K. L. Tsakmakidis, A. N. Askarpour, P. Dehkhoda, A. Tavakoli, H. Altug, *ACS Photonics* **2018**, *5*, 2669.
[27] J. García-Guirado, M. Svedendahl, J. Puigdollers, R. Quidant, *Nano Lett.* **2020**, *20*, 585.
[28] M. L. Solomon, J. Hu, M. Lawrence, A. García-Etxarri, J. A. Dionne, *ACS Photonics* **2019**, *6*, 43.
[29] R. Knipper, V. Kopecký, U. Huebner, J. Popp, T. G. Mayerhöfer, *ACS Photonics* **2018**, *5*, 3238.
[30] T. Iida, A. Ishikawa, T. Tanaka, A. Muranaka, M. Uchiyama, Y. Hayashi, K. Tsuruta, *Appl. Phys. Lett.* **2020**, *117*, 101103.
[31] C. Xu, Z. Ren, H. Zhou, J. Zhou, C. P. Ho, N. Wang, C. Lee, *Light: Sci. Appl.* **2023**, *12*, 154.
[32] H. Altug, S. H. Oh, S. A. Maier, J. Homola, *Nat. Nanotechnol.* **2022**, *17*, 5.
[33] A. Minopoli, A. Acunzo, B. D. Ventura, R. Velotta, *Adv. Mater. Interfaces* **2022**, *9*, 2101133.
[34] M. Janneh, *Results Opt.* **2022**, *6*, 100201.
[35] A. Tittl, A. Leitis, M. Liu, F. Yesilkoy, D. Y. Choi, D. N. Neshev, Y. S. Kivshar, H. Altug, *Science* **2018**, *360*, 1105.
[36] C. Soto, S. Pritzkow, *Nat. Neurosci.* **2018**, *21*, 1332.
[37] F. Chiti, C. M. Dobson, *Annu. Rev. Biochem.* **2006**, *75*, 333.
[38] T. A. Keiderling, *Curr. Opin. Chem. Biol.* **2002**, *6*, 682.
[39] C. Guo, R. D. Shah, R. K. Dukor, T. B. Freedman, X. Cao, L. A. Nafie, *Vib. Spectrosc.* **2006**, *42*, 254.
[40] D. Chanda, D. Franklin, A. Safaei, S. Modak, A. Vázquez-Guardado, *Opt. Lett.* **2018**, *43*, 6001.
[41] D. Chanda, S. Chandra, D. Franklin, A. Safaei, S. Modak, A. Vázquez-Guardado, J. Lee, *Opt. Express* **2018**, *26*, 32931.
[42] A. Vázquez-Guardado, D. Chanda, *Phys. Rev. Lett.* **2018**, *120*, 137601.
[43] A. Biswas, P. Cencillo-Abad, M. W. Shabbir, M. Karmakar, D. Chanda, *Sci. Adv.* **2024**, *10*, 2560.
[44] R. Adato, A. A. Yanik, J. J. Amsden, D. L. Kaplan, F. G. Omenetto, M. K. Hong, S. Erramilli, H. Altug, *Proc. Natl. Acad. Sci. USA* **2009**, *106*, 19227.
[45] F. Cheng, X. Yang, J. Gao, *Sci. Rep.* **2015**, *5*, 14327.
[46] F. Neubrech, A. Pucci, T. W. Cornelius, S. Karim, A. García-Etxarri, J. Aizpurua, *Phys. Rev. Lett.* **2008**, *101*, 157403.
[47] A. N. Schechter, *Blood* **2008**, *112*, 3927.
[48] P. Ferraboschi, S. Ciceri, P. Grisenti, *Antibiotics* **2021**, 10.